Downscaling potential evapotranspiration to the urban canyon

Merle Koelbing[1], Tobias Schuetz[2], Markus Weiler[1]

[1]Faculty of Environment and Natural Resources, University of Freiburg, Freiburg im Breisgau, 79098, Germany
[2]Faculty of Regional and Environmental Sciences, University of Trier, Trier, 54284, Germany

5   *Correspondence to*: Merle Koelbing (merle.koelbing@gmx.de)

Abstract

The future increase in urban population will lead to progressing urbanization with urban sprawl and densification. Urbanized areas show distinct changes in their hydrological behaviour, water quality and climate. In the last decades, the ability of urban hydrological models to represent the dynamic hydrological behaviour of the different surface types has been improved

10   continuously. Dissenting from the urban surface which is mostly represented in high spatial resolution, the climatic input to these models, such as precipitation and potential evapo(transpi)ration, is usually observed at one or several reference climate stations that are representing a mesoscale urban foot print area or rural conditions. From urban climate studies it is known, that the meteorological variables that are governing potential evapotranspiration (E_p) can be highly variable even on a small spatial scale. Consequently, we expect E_p at the street level to be affected by this variability as well.

15   We observed the urban microclimate with a mobile climate station and a rotational principle at 16 different locations in two differently oriented street canyons with vegetated and non-vegetated sections, respectively, during three seasons (spring, summer, autumn) in Freiburg, in southwestern Germany. With these observations, we simulated E_p at the street level using FAO-56 Penman-Monteith reference evapotranspiration and compared it to reference E_p derived at a rooftop station. We found that E_p on street level is negatively influenced by changes in shortwave radiation and that it is barely sensitive to changes in

20   the other input climate variables. Significant linear relationships between the relative differences in hourly and daily short-wave radiation input and E_p at the street level have been established. The application of these relationships allows to simulate E_p at the street level for any location in a city based on simulated (or observed) short wave time series and observations at a reference climate station. Our findings can be transferred easily to existing urban hydrologic models to improve modelling results with a more precise estimate of potential evapotranspiration on street level.

25   **1 Introduction**

By 2050, 68% of the world's and 84% of Europe's population are expected to live in cities (UN, 2018), starting from 55% worldwide and 74% in Europe in 2018 (UN, 2018). This increase in urban population will lead to progressing urbanization with urban sprawl and densification. Cities and urban areas already have a great impact on the water balance and on the hydrology of the receiving waters (Bonneau et al., 2017; Fletcher et al., 2013; Lerner, 2002; Schirmer et al., 2013). In contrast

30   to rural areas, fully or partly sealed surfaces in urban areas usually cause higher runoff, less groundwater recharge and lower evapotranspiration.

In the last decades, the ability of hydrological models to simulate the dynamic hydrological behavior of urban areas has increased continuously (Bach et al., 2014; Salvadore et al., 2015; Zoppou, 2001). Dependent on the purpose of each model, surface and soil characteristics as well as drainage via the sewer system controlling the hydrologic processes on the soil surface

35   and below ground are considered in detail in many urban hydrologic models. Even low impact development (LID) elements can be implemented in some models (see Elliot and Trowsdale (2007) for an overview of urban drainage models which are able to represent LID tools). In contrast to the spatially highly resolved information on the urban surface, the meteorological input for these models is still derived from observations with a mesoscale footprint area.

Determining the actual evapotranspiration (ET_a) of urban areas is demanding, in specific, in high spatial resolution for the area

40   of a whole city (Nouri et al., 2013). Adequate observations of actual evapotranspiration for a city under interest in the desired spatial and temporal resolution and extent are seldom available (Nouri et al., 2013). Even in cities with a high proportion of sealed surfaces evapotranspiration is a controlling component of the water balance, hence, it should not be neglected (Grimmond & Oke, 1999). To overcome the absence of ET_a observations, many urban hydrological modells simulate ET_a for the fraction of unsealed surfaces dependent on the potential evaporation (E_p) and the physical behavior of soils and plants (e.g.

45   Grimmond & Oke, 1991; Mitchell et al., 2001; Berthier et al., 2006; Rodriguez et al. 2000; Rodriguez et al., 2008). Input variables for E_p are usually derived from a reference climate station which is located e.g. in rural areas or typically for many cities at the airport close to the city or on a rooftop directly in the urban area under investigation. By using these mesoscale E_p rates, we neglect that climate variables can vary considerably within the city on a small spatial scale.

The urban microclimate has been investigated intensely in the last decades especially in terms of developing and implementing

50   potential mitigation strategies against heat in cities (Bärring & Mattsson, 1985; Bourbia & Awbi, 2004; Norton et al., 2015; Oke, 1988; Salata et al., 2016; Shashua-Bar & Hoffman, 2000). From these studies it is known, that the climate variables thatwhich influence E_p - air temperature, relative humidity, wind speed, short- and longwave radiation - may be highly variable on small spatial scales, depending on surface characteristics as building height, orientation and width of the street canyon (Bourbia & Awbi, 2004; Oke, 1988), the presence of vegetation (Shashua-Bar & Hoffman, 2000) etc..

55   To our knowledge, no urban hydrologic model allows to adjust E_p to the specific microclimate conditions of an urban area. The only related approach from the field of urban gardening, the landscape coefficient method (LCM) by Costello et al. (2000), includes a so-called microclimate coefficient (k_{mc}) which adapts E_p (FAO-56 Penman-Monteith reference evapotranspiration (Allen et la., 1998)) to the specific microclimatic conditions of an urban green space. Daily E_p is calculated with meteorological data from a reference climate station and is then multiplied by k_{mc}. This coefficient ranges between 0.5 and 1.4 and thereby

60   decreases or increases E_p depending on whether the location is e.g. shaded or influenced by strong winds, respectively (Costello et al., 2000). Generally, the estimation of k_{mc} is very subjective because of the scarcity of urban ET_a measurements (Costello et al., 2000) and so k_{mc} is chosen individually for each green space based on visual examination. Litvak & Pataki (2016) established a significant relationship between k_{mc} and the fractional tree canopy cover for several public lawns in Los Angeles, California. This study is restricted to lawns shaded by trees and excludes shade by buildings and the behavior of E_p in a more

65   heterogenic urban environment. Consequently, this method is still not directly applicable to urban hydrological modelling. Other procedures to downscale mesoscale E_p to the urban microscale could be to analyze the behavior of E_p for different urban microclimatic conditions, similar to a sensitivity analysis. Many sensitivity analyses have been performed on E_p in terms of adjustments in the water management that might be needed as consequences of climate change (Ambas & Baltas, 2012; Bormann, 2012; Gong et al., 2006; Sharifi & Dinpashoh, 2014; Tabari & Talaee, 2014) or in terms of estimation errors due to

70   measurement uncertainties or missing input data (Beven, 1979; Bois & Pieri, 2005; Debnath et al., 2015). Of those, only Beven (1979) analyzed variations below the diurnal resolution in an hourly time step. Since it is unknown whether the assumed changes in the input variables of formerly conducted sensitivity analyses are applicable in an urban setting, findings from these studies should not be used directly. The derivation of variation and cross-correlation of the micro-meteorolgical variables requires continuous observations of all input variables in high spatial and temporal resolution in an urban setting over a longer

75   time period. However, observing these variables in cities is very difficult due to the risk of vandalism and the lack of space for installing the sensors (Erell & Williamson, 2007; Oke, 2006). Further, it is very costly to establish a network of climate stations that represents the heterogeneity of a whole city (Erell & Williamson, 2007; Oke, 2006).

Mobile measurements are a novel way to gain highly resolved spatial information about the microclimatic conditions in cities without the disadvantages of a stationary observation network (Rajkovich & Larsen; 2016). For example, several point and

80   transect measurement campaigns examined the impact of different street and building designs on the urban heat/cool island phenomena and on human thermal comfort (Voogt & Oke, 1998; Blankenstein & Kuttler, 2004; Conrads & van der Hage,

1971; Chen et al., 2012; Tsin et al., 2016; Heusinkveld et al., 2014; Unger et al., 2001; Rajkovich & Larsen; 2016; Brandsma & Wolters, 2011). The sensors were mounted on bicycles (Brandsma & Wolters, 2011; Heusinkveld et al., 2014; Rajkovich & Larsen, 2016) and cars (Blankenstein & Kuttler, 2004; Conrads & van der Hage, 1971; Unger et al, 2001; Voogt & Oke, 1998)

85 or observations were carried out on foot (Chen et al., 2012; Tsin et al., 2016). It is also common to set up few portable stations at specific locations for several hours (Dimoudi et al. 2013; Holst & Mayer, 2011; Lee et al., 2013; Salata et al., 2016). Since these microclimate studies aim typically on heat mitigation and human thermal comfort, such mobile measurements often represent only short time periods of a few hours during specific weather conditions and do not cover all meteorological variables needed to simulate E_p. In addition, mobile equipment has to be supervised for the whole observation period or at

90 least has to be set up daily which leads to measurement campaigns with only a small number of replications.

In order to capture the spatial and temporal patterns of meteorological variables influencing the potential evapotranspiration in a complex urban environment, this paper presents the results of an intense monitoring study carried out in 2016 and 2017 with a mobile climate station mounted on a bicycle trailer, in Freiburg, Germany. The primary aim of this study was to develop an approach to downscale mesoscale or reference E_p observations to the urban microscale at the street level on a daily and

95 diurnal time scale.

2 Methods

2.1 Study area

Data were collected in two adjacent urban street canyons in Freiburg, southwestern Germany. Freiburg is located close to the Black Forest, 278 m above sea level, in a warm and humid temperate climate zone with mean annual air temperature and

100 precipitation of 11.4°C and 837 mm, respectively. The two streets selected as study sites are located in the residential district "Wiehre" - the street "Hildastraße" (HS), is north-south, the other street, "Erwinstraße" (ES), is east-west oriented, both intersecting each other. Four-storey buildings from the late nineteenth and early twentieth century line the streets generating the typical characteristics of an urban canyon. Both streets consist of sections with and without vegetation. In the vegetated sections, trees line the sidewalk and lawns, bushes and hedges grow in the front yards. The non-vegetated sections show no

105 vegetation at all, with sidewalks right in front of the buildings and parking lanes along both sides of the roads. Sidewalks and roads are fully paved in the vegetated and non-vegetated sections in both streets. Both streets offer distinctive boundary conditions due to their homogeneous building structure and their straight orientation. We selected in both streets one vegetated (v) and one non-vegetated (n) section for data collection. In HS the vegetated section is south, in ES it is east to the non-vegetated section. On the eastern side of the vegetated section in HS, the buildings stand back from the street and the area in

110 front of them is partly used as a front yard and small parking lot. Four trees (*Platanus*) are growing here along the road with approximately 12 m height and 10 m distance among each other. The canyon width in the northern and southern section is 13 m and 18 m, respectively. Houses are 15 m high at the rooftop in the northern and 18 m in the southern section. In the vegetated section of ES there are front yards with shrubs and partly with hedges on both sides of the street in front of the buildings. A few black locust trees (*Robinieae*) grow on grass strips along the road. Parking lanes are also along both sides of

115 the road (Fig. 1). Canyon width in the western and eastern section is 12 m and 24 m respectively. Houses are 18 m high at the rooftop in both sections.

In each street, eight measurement locations were selected (Fig. 2). The locations were situated on the sidewalks approximately 50 cm away from the curb. In HS, four locations were selected in each section, two on each side of the road respectively. In ES, two locations were selected in the vegetation free section, one on each side of the road, and six in the vegetated section,

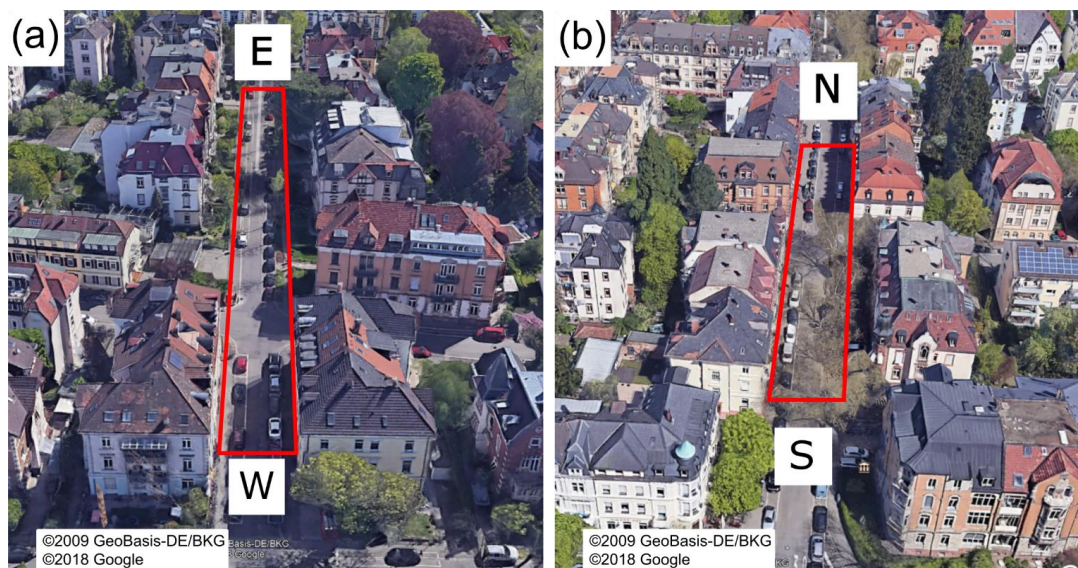120 three on each side of the road, respectively.

Figure 1: (a) ES from west to east (non-vegetated section in front), (b) HS from south to north (vegetated section in front).
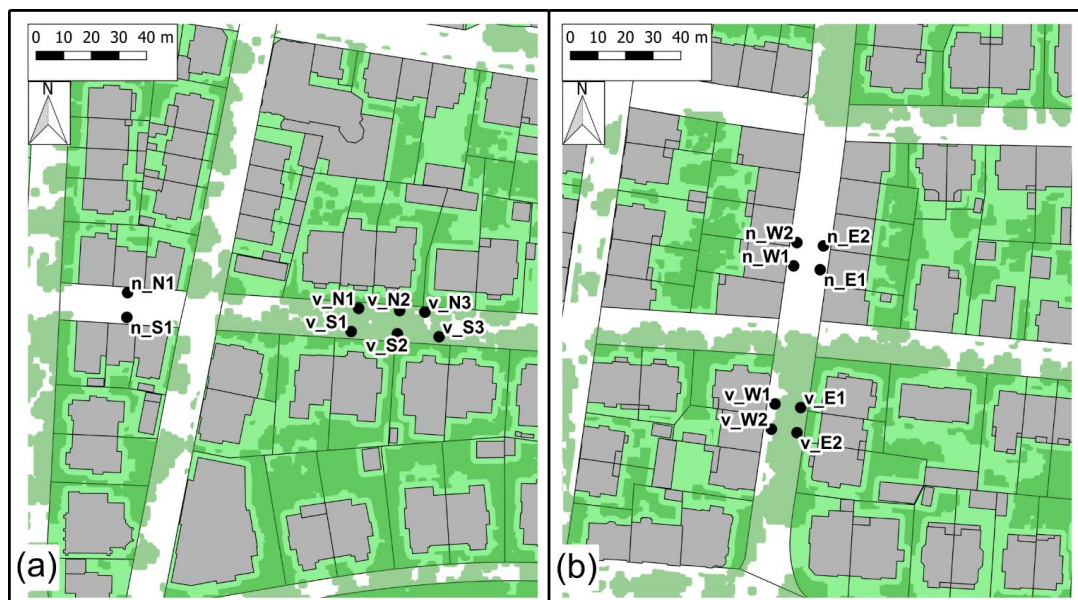

Figure 2: Measurement locations in (a) ES and (b) HS. Buildings in grey, non-paved areas (mainly gardens) in bright green, trees
125   and shrubs in dark green.

2.2 Observations

We performed microclimatic measurements with a mobile climate station, mounted on a bicycle trailer. We pulled the trailer
by bike to the streets and moved it around by hand to the measurement locations within the streets. We observed air temperature
(T_a), relative humidity (rh), wind speed (u), incoming shortwave radiation ($K\downarrow$) as well as the infrared surface temperature of
130   the ground ($T_{s,ground}$), the four cardinal directions ($T_{s,NESW}$) and from above ($T_{s,up}$) (Table 1, Fig. 3). $T_{s,NESW}$ and wind sensors
are fixed at a vertical pole which was adjusted vertically and oriented to the cardinal points by a ball joint in order to adjust
the sensors quickly without moving the whole trailer. $T_{s,NESW}$ sensors are fixed high enough so the trailer does not appear in
the field of view (FOV) of the sensors. We attached the up- or downward pointing sensors at the end of an extension bar, which

was also fixed to the vertical pole. When the vertical pole is oriented correctly, the extension bar is pointing south to avoid

135   shadow from the vertical pole. The sensors at the extension bar are fixed 160 cm away from the vertical pole so the trailer platform does not appear in the FOV of the $T_{s,ground}$ sensor. The measurement interval was set to 7.5 seconds and data were logged every 15 seconds as the arithmetic mean of two observations.
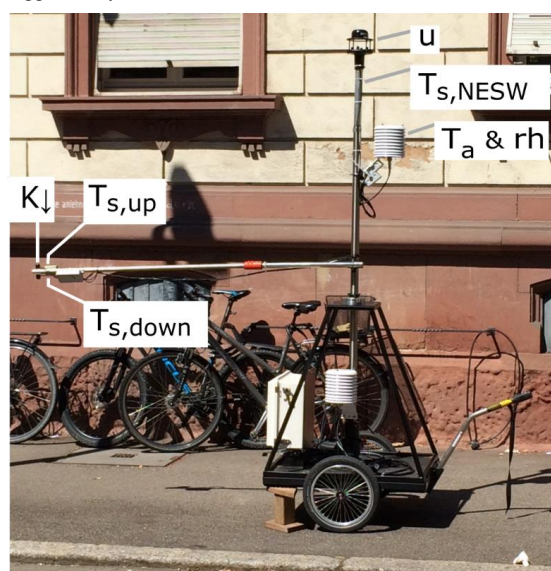
Figure 3: Mobile climate station located at n_W1.

140   The measurement locations in each street were visited consecutively in the same order in a rotational principle. Within one hour, we ensured a 4-minute measurement at all measurement locations in one street including the time to move the trailer between the locations and the rearrangement of the mobile climate station. After each 4-minute interval, i.e. while moving to the next location and rearranging the station, the logger was switched off. Observations were carried out throughout the day for several days in three different seasons (spring, summer and autumn) in the years 2016 and 2017 in each street (Table 2).

145   Since we only had one mobile climate station available, both streets were observed one after the other in each season. The daily observation period in each season started approx. two hours after sunrise and ended two hours before sunset.

Since the conditions at each measurement location might change within one hour (heating/cooling, sunny/shaded), we varied the starting point of the rotation from day to day, meaning, one measurement location might be visited early in each hour on one day but late on the other, thus we can catch as much of the variety as possible.

150   We did not account for changing weather conditions within the season, meaning that we observed sunny and dry conditions as well as wet and cold conditions. However, we had to interrupt the observations under harsh weather conditions such as heavy rain or strong wind to avoid damage on the electronic parts or if technical issues resulted in measurement problems. Hence, the samples for calculating hourly averages per season and measurement location might originate from different days and vary in size (Fig. 4). At the end of each observation day, the data was read out and edited manually, e.g. to delete data of periods

155   during which the logger was only switched on to check the device or by accident. We created one metafile for each street and season containing the dates of the observation days, the number of rotations and the starting point of the day as well as if locations had to be skipped in a specific hour which happened mainly because the observations had to be interrupted, started late or ended early.
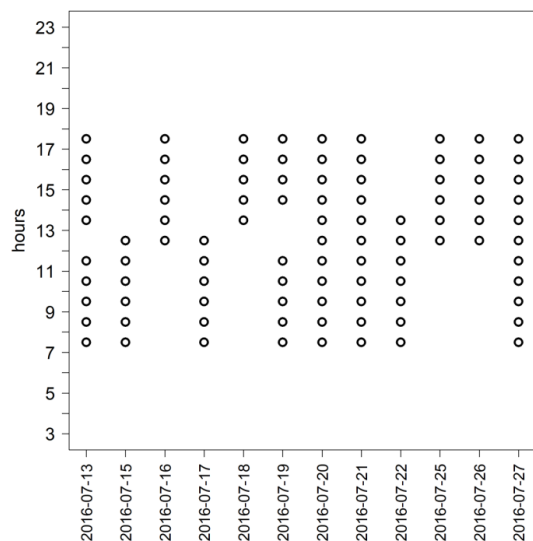
Figure 4: Example of observation times for HS in summer. Each dot represents a full rotation, i. e. 4 min. of measurements at each of the eight locations.

Table 1: Technical details of the sensors mounted on the mobile climate station trailer.

| Variable	Unit	Sensor	Height above top ground surface	Accuracy	Response time / Field of view (FOV)
T_a	[°C]	Campbell CS215	200 cm	0.4°C	120 s / -
rh	[%]	Campbell CS215	200 cm	2 %	120 s / -
u	[m s^{-1}]	Gill WindSonic 2D	2 cm	2 %	- / -
T_s	[°C]	Melexis MLX90614	115 cm (ground/up) 215 cm (NESW)	0.5 °C	- / 90°
$K_\downarrow$	[W m^{-2}]	Apogee Sp110 Pyranometer	115 cm	5 %	- / 180°

Table 2: Seasonal and daily observation period for each street. N_d is the number of days on which measurements took place; n is the total number of 4-minute observations; $\bar{n}$ is the mean number of observations per measurement location; $\bar{\bar{n}}$ is the mean number of observations per measurement location per hour.

Season	Street	Measurement Period		Daily Timespan (CET)	N_d	n	$\bar{n}$	$\bar{\bar{n}}$
		Year	Month/Day					
Spring	HS	2016	04/01 – 04/14	08:00 – 16:00	10	481	60	7.5
	ES	2017	03/28 – 04/11		10	620	78	9.8
Summer	HS	2016	07/13 – 07/27	07:00 – 18:00	12	689	86	7.8
	ES	2016	07/28 – 08/05		11	429	54	4.9
		2017	07/31 – 08/07					
Autumn	HS	2016	10/31 – 11/24	09:00 – 16:00	12	570	71	10.1
	ES	2016	11/21 – 12/16		16	625	78	11.2

We used two reference climate stations for permanent climate observation. One is located on a flat roof approximately 15 m above street level and 2.5 km distance south-west from the study area in a similar urban area. It observes Ta, rh, K↓ and u

170   continuously with a time step of one minute. The second reference station observes K↓ with a 10-minute time step and is located on a high-rise, 52 m above ground, 2 km distance north from the study area. We used the K↓ data from the high-rise station because we had foggy conditions in winter and spring in the morning hours at the other station while in the streets, we observed clear sky conditions. The continuous reference observations allow to correct for the changes in the system over time when comparing the microclimatic conditions between the single measurement locations. By choosing reference stations which

175   are also located in the city, we avoid observing an urban-rural difference of the atmospheric condition (Nunez et al., 2000; Blankenstein & Kuttler, 2004) which is not subject of this study.

In addition to the meteorological observations we derived the sky view factors Ψ_{sky} for each measurement location in each season by taking pictures pointing vertically towards the sky using a NIKON D5100 camera with a SIGMA 4.5 mm F2.8 EX DC fish-eye lens with 180° opening angle. The pictures were taken at 115 cm height which is the same as for the upward

180   pointing sensors. We used ImageJ (https://imagej.nih.gov/ij/index.html, last visited 13 July 2020) software to derive binary images with white pixels representing sky and black pixels representing obstacles (example in Fig. 5). We achieved this by setting thresholds in the brightness of the pictures and/or by rendering the obstacles manually. Ψ_{sky} was then calculated using the RayMan model (Matzarakis et al., 2007; Matzarakis et al., 2010) which relates the number of sky-pixels to the total number of pixels in the image, considering the image is representing a hemisphere.

185
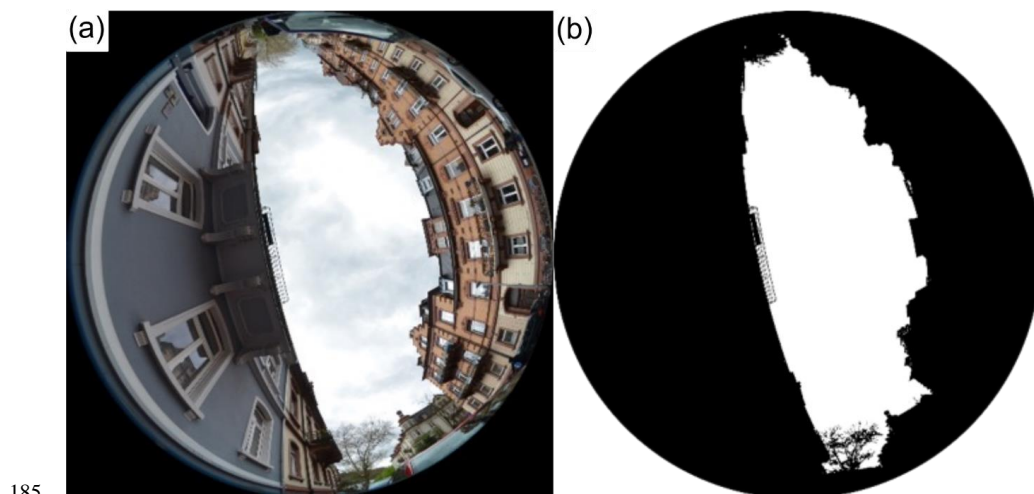
Figure 5: Sky view at location n_E1 in HS. (a) fish eye photo with 180° FOV. (b) corresponding binary image with white pixels representing the sky and black pixels representing elements corresponding to $\Psi_{sky} = 0.26$.

2.3 Data Analysis

With the data set created with our observations we were able to calculate hourly potential evaporation rates for the measurement

190   locations ($E_{p,s}$) and corresponding hourly potential evaporation rates for the reference station ($E_{p,r}$). We treated the mean of each 4-minute measurement as a representative sample of the hourly mean. We selected the corresponding reference observation at the same time and treated it as an hourly mean instead of working with the "real" hourly mean at the reference station. Giving each observation at each measurement location its "own" reference value avoids mixing temporal and spatial signals. For the 1-minute reference observations we took exactly the same minutes in which the mobile observation took place

195   (Fig. 6). For the reference solar radiation observations with 10-minute time steps, we selected the 10-minute time step in which the mobile observation laid in. When the mobile observation exceeded one 10-minute time step, we took the mean value of both time steps as a reference.
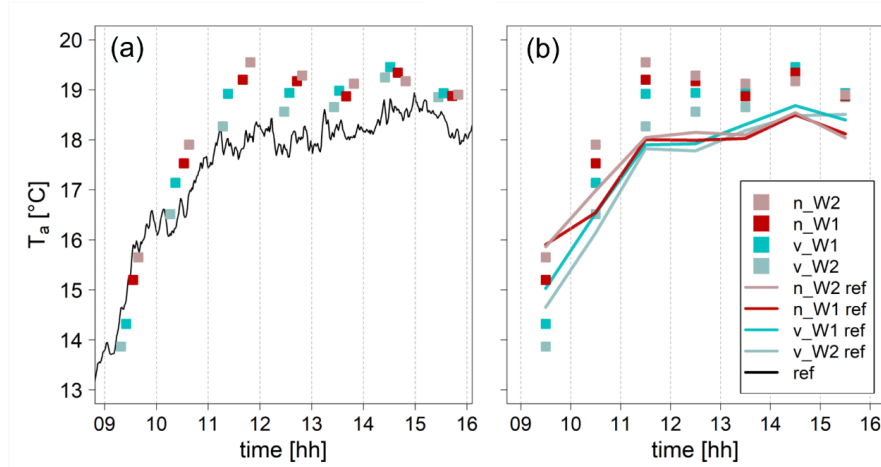
Figure 6: Observations on 3 April 2016 as an example of adjusting observations of the mobile and the reference station. (a) 4-minute observations of T_a at the different measurement locations at the western side of HS and continuous T_a reference observation (black); (b) 4-minute observations of T_a at the different measurement locations at the western side of the road with corresponding reference values picked from the continuous rooftop observation as representative sample of the hourly mean.

For all measurement locations and the observations at the reference stations, FAO-56 Penman-Monteith reference evapotranspiration (Allen et al., 1998) was calculated with Eq. (1). Assuming that most urban green spaces consist mainly of

205 well-maintained turf grass, the FAO-56 Penman-Monteith reference evapotranspiration (evapotranspiration "from an extensive surface of green grass of uniform height, actively growing and adequately watered" (Allen et al., 1998)) seems to be a suitable estimator for the potential evapotranspiration from these surfaces under the given atmospheric conditions. For simplifying the denotation later, we refer to it as E_p:

$$E_p = \frac{0.408 * \Delta * (Q^* - Q_G) + \gamma * \frac{37}{T_a + 273} * u * (e_s - e_a)}{\Delta + \gamma * (1 + 0.34 * u)} \ [\text{mm h}^{-1}] \tag{1}$$

210 with:

	Q^*	net radiation at crop surface [MJ m^{-2} h^{-1}]
	Q_G	soil heat flux density [MJ m^{-2} h^{-1}]
	T_a	mean hourly air temperature at 2 m height [°C]
	u	mean hourly wind speed at 2 m height [m s^{-1}]
	e_s	saturation vapor pressure at air temperature [kPa]
215		e_a	mean hourly actual vapor pressure [kPa]
	Δ	slope of the saturation vapor pressure curve [kPa °C^{-1}]
	γ	psychrometric constant [kPa °C^{-1}]

Parameters characterizing the surface of the measurement locations were kept constant representing a reference grass surface independent of the real surface at each location to allow comparison at all locations independent of the mix of real surfaces.

220 Consequently, differences in E_p among measurement locations originate from differences in meteorological conditions. Additionally, we adapted Eq. 1 to not only observe the impact of the climate variables but also the longwave radiation influence of each location from buildings and trees. In Allen et al. (1998) the net outgoing longwave radiation L^* is modelled on the basis of T_a, rh and $K_\downarrow$ without differentiating between incoming and outgoing longwave radiation ($L_\downarrow$ and $L_\uparrow$ respectively):

$$L^* = \sigma * (T_a + 273.15)^4 * (0.34 - 0.14 * \sqrt{e_a}) * (1.35 * cc - 0.35) = L_\uparrow - L_\downarrow \ [\text{MJ m}^{-2} \text{h}^{-1}] \tag{2}$$

225 with:

	L^*	net outgoing longwave radiation
	σ	Stefan–Boltzmann constant 5.67 x 10^{-8} [W m^{-2} K^{-4}]
	$K_{0\downarrow}$	extraterrestrial solar radiation [MJ m^{-2} h^{-1}]
	cc	clearness index

Hydrology and
Earth System
Sciences
Open Access
Discussions
EGU

	L↑	outgoing longwave radiation
230	L↓	atmospheric counter radiation

The clearness index is defined as cc = $K_{\downarrow r}/K_{\downarrow 0}$ where $K_{\downarrow r}$ is solar global radiation observed at the reference station and $K_{\downarrow 0}$ is the exoatmospheric shortwave radiation at a horizontal surface (Offerle et al., 2007). With rearranging Eq. (2), $L_\downarrow$ and $L_\uparrow$ could be modelled separately resulting in $L_\downarrow$ being the atmospheric counter radiation for an unobstructed hemisphere:

$$L_\downarrow = L_\uparrow - L^* = \sigma * (T_a + 273.15)^4 * \varepsilon_{grass} - L^* \text{ [MJ m}^{-2}\text{ h}^{-1}]$$ (3)

235 ε_{grass} is the emissivity of a grass surface according to FAO-56 Penman-Monteith reference evapotranspiration (Allen et al. 1998) and was set to ε_{grass} = 0.98 (Matsui & Osawa, 2015). Input for L^* and $L_\downarrow$ was taken from the reference stations as the measurements are not influenced by surrounding objects and we assume that the atmospheric conditions are the same for the whole city area (Blankenstein & Kuttler, 2004).

In a next step, we included the longwave input from the urban surroundings in the calculation of incoming longwave radiation
240 by using the observed infrared radiation surface temperatures. The infrared sensors measured the integrated infrared radiation surface temperature for all "seen" surfaces (T_s). At some measurement locations, the lateral infrared sensors also "saw" the ground, which in relation to the radiation balance represents an outgoing term of radiation, while we were interested in the incoming longwave radiation. Therefore, we had to subtract the part of the infrared radiation surface temperature originating from the ground. We took additional fish eye photos from each cardinal direction and corrected them for a 90° opening angle
245 to represent the FOV of the infrared sensors (Fig. 7). We calculated the fraction of the ground in the FOV and refer to it here as the ground view factor of the infrared sensors (Ψ_{ground}). We calculated Ψ_{ground} by simply relating the number of pixels showing the ground to the total number of pixels of the "flat" circle.
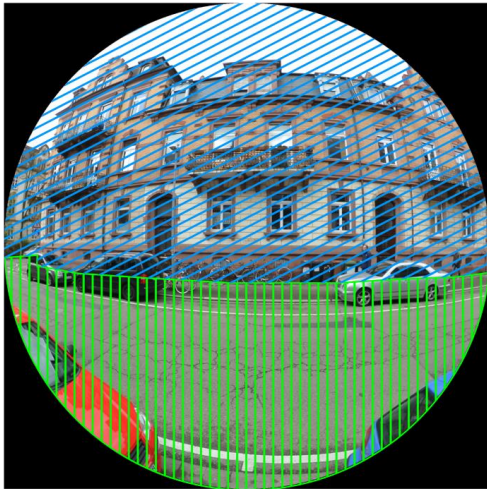
Figure 7: Fish eye photo representing the 90° FOV of the T_s sensor in HS at n_E1 pointing west. Green: ground, representing $L_\uparrow$;
250 **blue: sky and buildings, representing $L_\downarrow$.**

Using Ψ_{ground} and $T_{s,ground}$ observed by the downward pointing infrared sensor, it was then possible to subtract the infrared radiation surface temperature of objects and sky ($T_{s\downarrow}$). This was done for each sensor at all locations for each time step with

$$T_{s\downarrow} = \frac{T_s - \Psi_{ground} * T_{s,ground}}{(1 - \Psi_{ground})} \text{ [°C]}$$ (4)

as a transformation of

255 $$T_s = \Psi_{ground} * T_{s,ground} + \left(1 - \Psi_{ground}\right) * T_{s\downarrow} \text{ [°C]}$$ (5)

The mean "incoming" infrared radiation temperature for the whole hemisphere at each measurement location ($\overline{T_{s\downarrow}}$) can then be derived as the arithmetic mean from the four cardinal directions and the upward pointing sensor:

$$\overline{T_{s\downarrow}} = \frac{\sum T_{s\downarrow}}{5} \text{ [°C]}$$ (6)

Since the ground surface cannot be seen by the upward pointing sensor, the observed T_s is equivalent to $T_{s\downarrow}$ for this sensor. We

260   finally calculated incoming longwave radiation at the measurement locations ($L_{\downarrow s}$) by:

$$L_{\downarrow s} = \Psi_{sky} * L_\downarrow + \left(1 - \Psi_{sky}\right) * \varepsilon_{obj} * \sigma * (\overline{T_{s\downarrow}} + 273.15)^4 \text{ [MJ m}^{-2}\text{ h}^{-1}] \qquad (7)$$

with ε_{obj} being the emissivity of the surrounding objects. We selected $\varepsilon_{obj} = 0.97$ on the basis of a study conducted by Verthegy

& Munro (1989) who measured the longwave emissivity of a variety of surface materials.

Modelling $E_{p,s}$ with a separate term for $L_{\downarrow s}$ instead of the net radiation given in Eq. (2) is necessary because otherwise $K_{\downarrow s}$,

265   which is highly influenced by the shading of buildings and trees, would lead to a wrong calculation of the clearness index and

consequently to wrong estimations of net longwave radiation at the measurement locations (see Eq. (39) in Allen et al. (1998)

and its description). As recommended by Allen et al. (1998) the minimal wind speed was set to 0.5 m/s. All calculations were

done for hourly time steps assuming the 4-minute-measurement being representative for the hour the measurement was taken

in. If not mentioned otherwise, parameters were taken from Allen et al. (1998) and wind speed measurements at the roof top

270   station were corrected for the sensor height of 15 m with a zero-plane displacement length of d = 1 m after Eq. (47) in Allen

et al. (1998).

To investigate the behavior of E_p in the street ($E_{p,s}$) in relation to the reference ($E_{p,r}$) we decided to display the results as the

difference between $E_{p,s}$ and $E_{p,r}$ relative to the absolute $E_{p,r}$ value and call it the relative difference of E_p with:

$$\delta E_p = \frac{E_{p,s} - E_{p,r}}{|E_{p,r}|} = \frac{\Delta E_p}{|E_{p,r}|} \text{ [-]} \qquad (8)$$

275   If $E_{p,r} < 0$ or $E_{p,s} < 0$ there are condensation conditions at the reference station or in the street, respectively.

To derive average daily sums of $K_\downarrow$ and E_p (for street and rooftop), we first calculated for each measurement location in each

season the average hourly values and summed these up to a daily (daytime) sum. With these, we calculated daily $\delta K_\downarrow$ and δE_p

according to Eq. (8).

$$E_{p,OAAT} = \begin{cases} E_p\left(\boldsymbol{T_{a,s}};\, rh_r;\, u_r;\, K_{\downarrow r};\, L_{\downarrow r}\right) & \text{if } OAAT = T_a \\ E_p\left(T_{a,r};\, \boldsymbol{rh_s};\, u_r;\, K_{\downarrow r};\, L_{\downarrow r}\right) & \text{if } OAAT = rh \\ E_p\left(T_{a,r};\, rh_r;\, \boldsymbol{u_s};\, K_{\downarrow r};\, L_{\downarrow r}\right) & \text{if } OAAT = u \\ E_p\left(T_{a,r};\, rh_r;\, u_r;\, \boldsymbol{K_{\downarrow s}};\, L_{\downarrow r}\right) & \text{if } OAAT = K_\downarrow \\ E_p\left(T_{a,r};\, rh_r;\, u_r;\, K_{\downarrow r};\, \boldsymbol{L_{\downarrow s}}\right) & \text{if } OAAT = L_\downarrow \end{cases} \qquad \text{[mm h}^{-1}] \qquad (9)$$

280   When substituting $E_{p,s}$ by $E_{p,OAAT}$ in Eq. (8) we receive $\delta E_{p,OAAT}$ showing the relative difference between $E_{p,OAAT}$ and $E_{p,r}$.

3 Results

Mean diurnal variations of E_p rates derived from continuous reference observations during each observation period show

expected values for our region (Fig. 8). It is noticeable that E_p rates in spring during the ES observation period were relatively

high due to consistently sunny and warm weather conditions (Table 3). The days (or half days) chosen for mobile data

285   collection were overall representative for each observation period. During the observation periods in HS, we slightly

overestimated E_p (Table 3). For observations in ES in summer, we unintentionally selected days that were sunny in the morning

but became cooler and cloudier in the afternoon which led to an underestimation of afternoon E_p rates. Daily observation

durations in spring were short compared to summer and autumn or rather started and ended too early since observations were

not distributed symmetrically around the midday maximum.
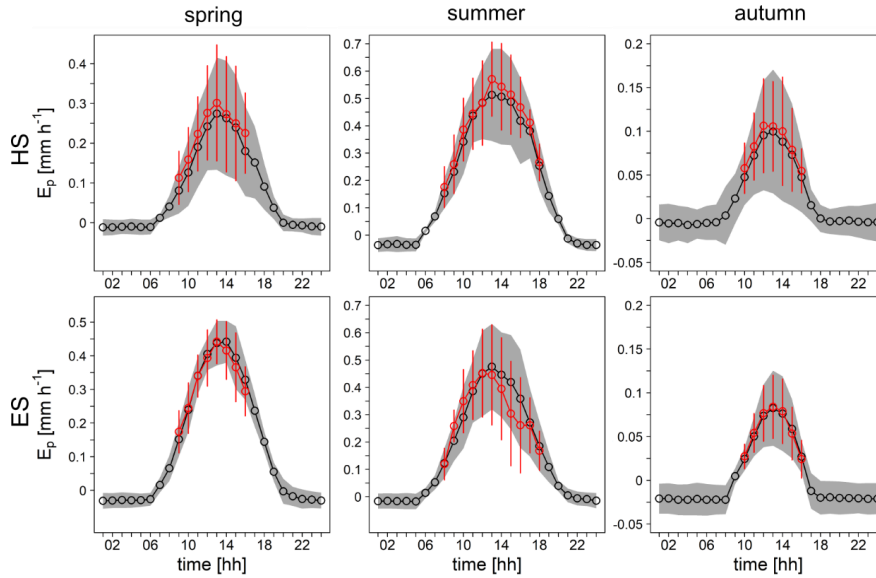
Figure 8: Mean diurnal variation of E_p for both streets for the three seasons. The black solid lines show E_p derived from continuous observations at the roof top stations during each seasonal observation period. The red solid lines depict $E_{p,r}$ only for hours during which microclimatic observations took place. Grey shadows/red error bars indicate the standard deviation.

Table 3: Sums of mean hourly daytime (day) and of mean hourly nighttime (night) E_p according to Fig. 8. $E_{p,cont}$ was derived from continuous observations at the reference station during each seasonal observation period and $E_{p,r}$ represents only hours during which microclimatic observations took place. Daytime represents the observations during daylight conditions in each season given in Table 2. Nighttime means all hours that are not included in the daily observation time span. Standard deviation in italic.

	spring			summer			autumn		
	$E_{p,r}$	$E_{p,cont}$		$E_{p,r}$	$E_{p,cont}$		$E_{p,r}$	$E_{p,cont}$	
	day	day	night	day	day	night	day	day	night
HS	1.8	1.6	0.2	4.5	4.2	0.0	0.6	0.5	0.0
	±0.3	*±0.3*	*±0.1*	*±0.4*	*±0.4*	*±0.1*	*±0.1*	*±0.1*	*±0.1*
ES	2.7	2.7	0.2	3.4	3.6	0.1	0.4	0.4	-0.3
	±0.2	*±0.2*	*±0.1*	*±0.4*	*±0.4*	*±0.1*	*±0.1*	*±0.1*	*±0.1*

The comparison between street and reference observations of the different input variables showed no significant difference for T_a and rh (displayed and tested as vapor-pressure deficit), with values distributed evenly close around the 1:1-line for all three seasons (Fig. 9). We used a one-sided t-test to test if the street observations of each variable (both streets, all three seasons) are different to its observed mean at the roof top stations. Wind speed in the streets was generally lower but sometimes higher and $L_\downarrow$ in the streets was nearly always higher than at the reference station. The largest influence of the urban surroundings can be seen for $K_\downarrow$, where most of the street observations are below the reference values. The differences between reference and street observations are significant at the 5% level for u, $L_\downarrow$ and $K_\downarrow$.
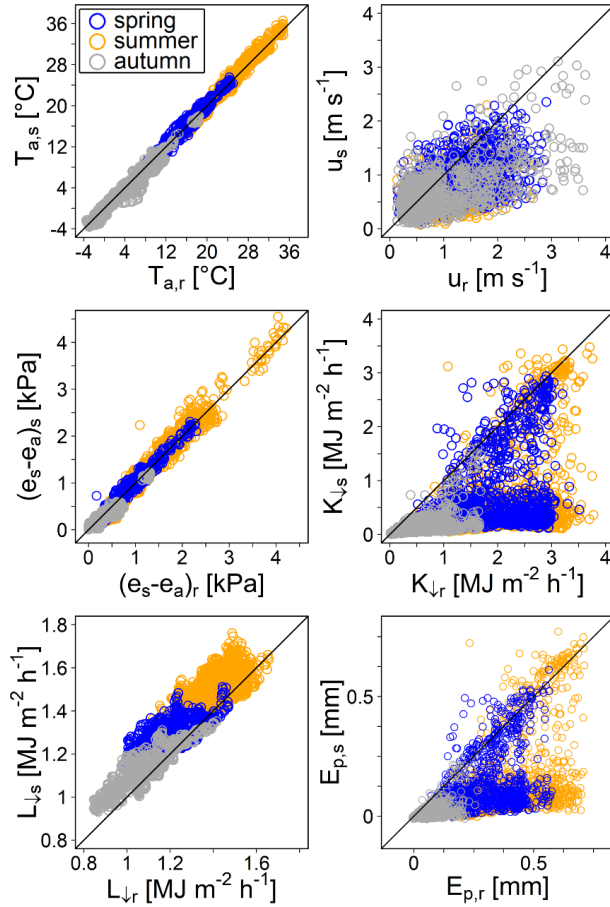
Figure 9: Street observations against reference observations of all locations in both streets in all three seasons. Observations of relative humidity are displayed as the vapor-pressure deficit e_s-e_a [kPa]. Black line represents 1:1-line.

The strongest correlation between meteorological variable and derived E_p can be observed for $K_\downarrow$ with a Spearman's rho of

310    $r_{K\downarrow,s} = 0.93$ for the street observations and $r_{K\downarrow,r} = 0.96$ for the reference observations (Fig. 10). For all other variables, we calculated positive, but weaker correlations. In the streets, the correlation between $L_{\downarrow,s}$ and $E_{p,s}$ with $r_{L\downarrow,s} = 0.62$ is very similar to that for vapor pressure deficit ($r_{(es-ea)s} = 0.69$) and air temperature ($r_{Ta,s} = 0.67$). We found the weakest correlation between u_s and $E_{p,s}$ with $r_{u,s} = 0.33$. For the reference observations we found very weak correlations between $E_{p,r}$ and $L_{\downarrow,r}$ with $r_{L\downarrow,r} = 0.41$ and wind speed with $r_{u,r} = 0.43$. Correlations are quite strong between $E_{p,r}$ and vapor pressure deficit ($r_{(es-ea)r} = 0.84$) and

315   air temperature ($r_{Ta,r} = 0.81$). Between street and reference observations, the correlation coefficients for $L_\downarrow$ differ the most. All correlation coefficients are lower for the street than for the reference observations, except $r_{L\downarrow}$, which is higher for the street observations.
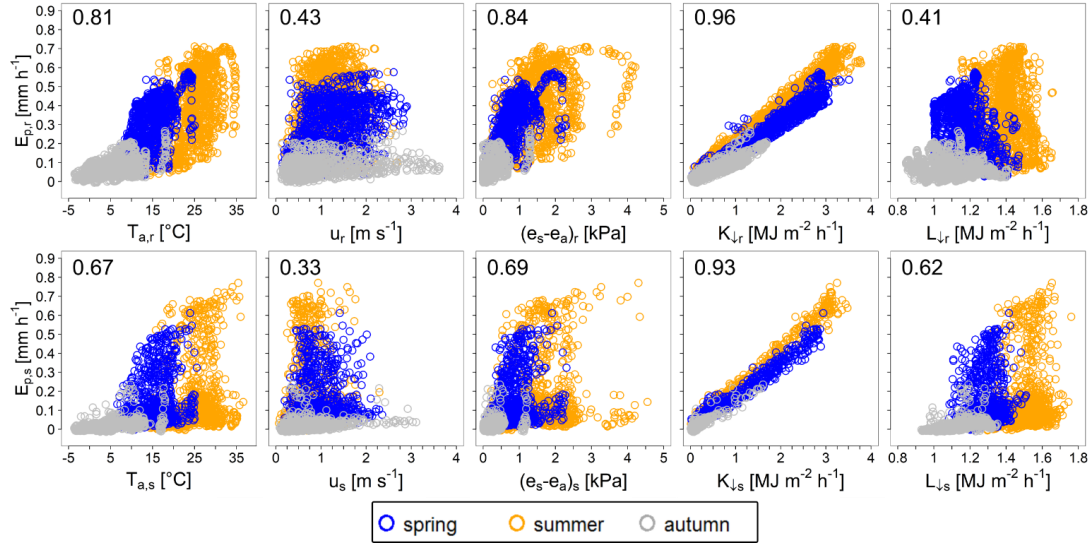
Figure 10: $E_{p,r}$ (top row) and $E_{p,s}$ (bottom row) in relation to the observed street and reference input variables, respectively. Overall data for all locations in both streets for all three seasons. Relative humidity is displayed as vapor pressure deficit. Numbers in the top left corner show Spearman's rho correlation coefficient.

Overall, $E_{p,s}$ is lower than $E_{p,r}$ for nearly all measurement locations in all seasons throughout the day which is indicated by negative values for $\overline{\delta E_p}$ (Fig. 11). The lowest $\overline{\delta E_p}$ (mean hourly) values from each season and each street range from -1.01 (ES, summer, v_S3, 7:00h) to -0.87 (HS, spring, n_E2, 8:00h and HS, autumn, n_W2, 15:00h). The highest $\overline{\delta E_p}$ values range from -0.50 (ES, autumn, v_S2, 12:00h) to 0.16 (ES, spring, v_N2, 8:00h). The results show a clear difference in the diurnal variation of $\overline{\delta E_p}$ among measurement locations that are at different sides of the road or in different sections of the streets (v / n). The observed patterns depict the insolation at each measurement location with, for example, sunny conditions at n_W2 in HS in the morning in spring with $\overline{\delta E_p}$ rising close to 0 and shaded conditions in the afternoon with $\overline{\delta E_p}$ dropping close to -0.90. In ES, n_S1 is shaded nearly throughout the day, even in summer except for the first hour of observation. Accordingly, $\overline{\delta E_p}$ at this measurement location is low compared to the other locations in ES. The shading effect on $\overline{\delta E_p}$ can also be seen when observations in summer of HS are compared to observations in spring. The patterns for measurement locations in the non-vegetated section are very similar to each other. But for the measurement locations in the vegetated section, we observed much lower $\overline{\delta E_p}$ in summer when the trees were in leaf and therefore this section receives less sunshine than in spring.
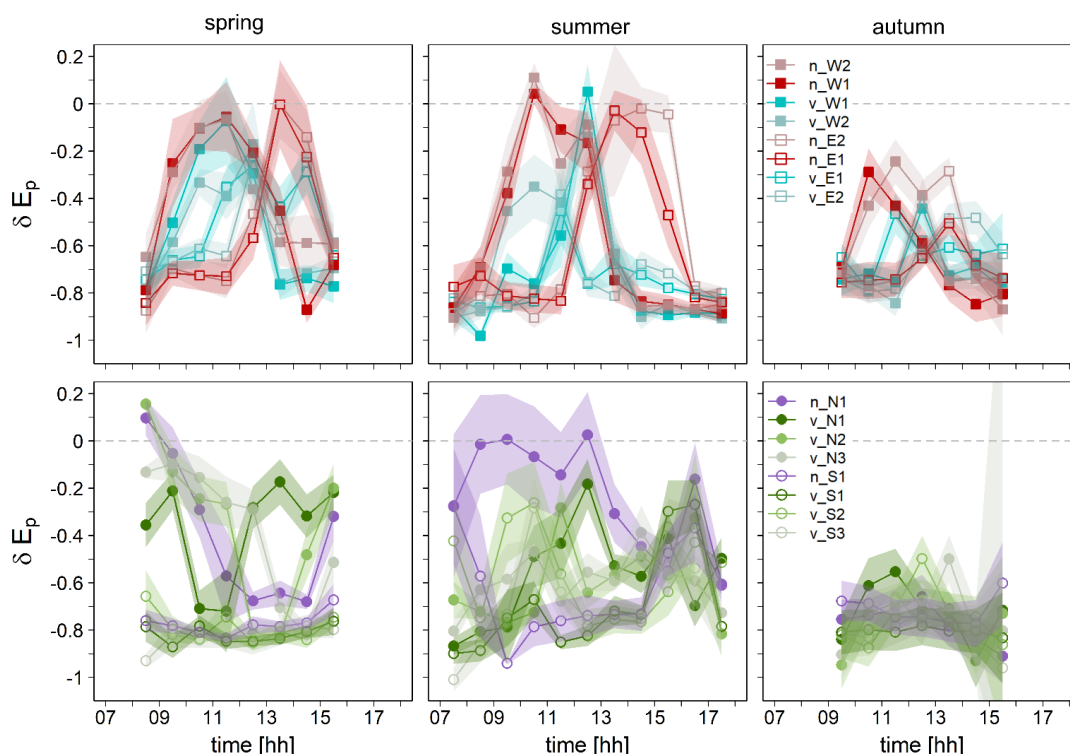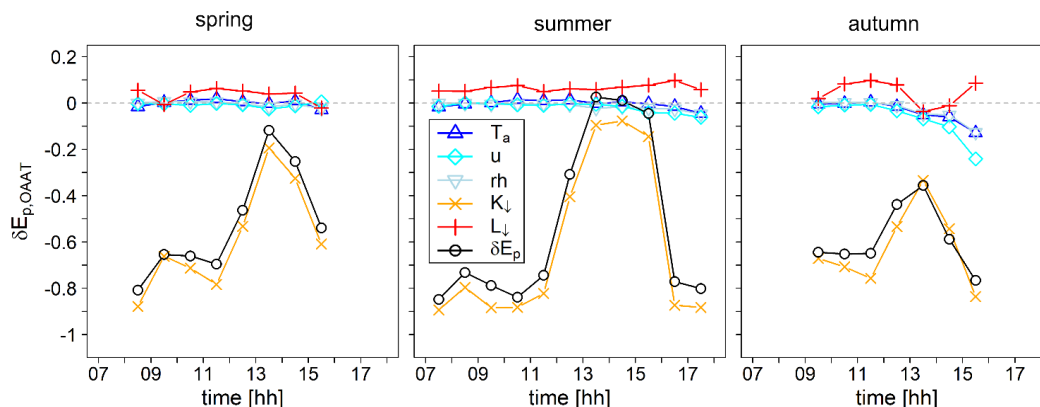
Figure 11: Mean diurnal variation of δE_p for each measurement location and each season with standard errors as shaded areas in HS (top) and ES (bottom), respectively.

In addition to the observed distinct diurnal variation of δE_p, also $\delta K_\downarrow$ and ΔT_a showed diurnal variations that were dependent on the position of the measurement location. The diurnal variation of shortwave radiation at the different measurement locations represents the shading by buildings and trees. For example, in HS on a sunny day in summer, $\delta K_\downarrow$ at v_W1 rises after 12:00h when the sun emerges from the trees and drops after 13:00h, when the sun disappears behind the building (Fig. 12). At n_W2, where no trees are shading the sun, the sun emerges already at around 09:00h which causes an earlier rise in $\delta K_\downarrow$ compared to v_W1. Consequently, the measurement locations show different diurnal patterns of ΔT_a due to different inputs of shortwave radiation: On a hot and sunny summer day, we observed the largest difference in ΔT_a at 12:30h, when ΔT_a at v_E1 (which was shaded by trees and by a building in the morning) was 2.1°C below ΔT_a at n_W2 (Fig. 12). Three hours later at the same day, we found a similar large difference in ΔT_a with v_W1 being the cooler site with ΔT_a being 1.8°C below ΔT_a at n_E1. Since the two locations with the biggest differences between ΔT_a are in different street sections and additionally, on opposite sides of the road, we can assume that this maximum "cooling effect" is caused by both, shade by vegetation and shade by building.
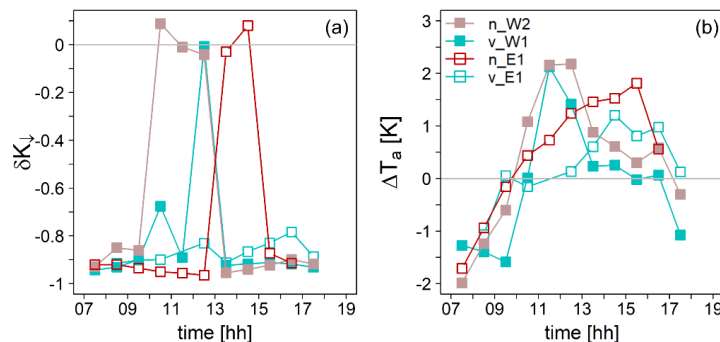
Figure 12: diurnal variation of (a) $\delta K_\downarrow$ and (b) ΔT_a [K] on 2016/07/20 in HS for four representative measurement locations.

The one-at-a-time analysis showed a strong sensitivity of E_p to changes in $K_\downarrow$. During the daily observation period in all three seasons, $\overline{\delta E_{p,K\downarrow}}$ is very close to $\overline{\delta E_p}$ (including all variables observed in the street), i. e. the replacement of $K_{\downarrow r}$ by $K_{\downarrow s}$ causes nearly the same change in $E_{p,r}$ as the replacement of all variables at once (see example in Fig. 13). For the other variables in all three seasons, $\overline{\delta E_{p,OAAT}}$ is close to 0, except for $L_\downarrow$, where a maximum $\overline{\delta E_{p,L\downarrow}}$ of 0.1 could be observed during autumn.

Figure 13: Mean diurnal variation of $\delta E_{p,OAAT}$ at n_E1 in HS. Colored lines: the naming variable is observed at n_E1, all other variables are from the roof top stations. Black line corresponds to δE_p with all variables observed at n_E1.

In order to quantify the high sensitivity of E_p to changes in $K_\downarrow$, we applied a linear regression between $\delta K_\downarrow$ and δE_p (Fig. 14). We excluded all cases when $\delta K_\downarrow > 0$ from the regression analysis because we assumed these cases are mainly affected by the measurement design (shading by clouds at the reference station but not in the street canyon). We established the linear regression with normalized $E_{p,r}$ rates (scaling between 0 and 1) to give more/less impact to observations in seasons, where potential evapotranspiration is actually higher/lower and therefore plays a bigger/smaller role in the annual water balance. Additionally, the relationship of average daily $\delta K_\downarrow$ and δE_p for each measurement location in each season was determined (Fig. 14). $\delta K_\downarrow$ ranges between -0.96 and -0.00 for hourly, and between -0.85 and -0.40 for average daily values. For both linear regressions with hourly and daily data we achieve very good fits (R²=0.94/0.96, respectively) with slopes close to 1 (b=1.07/1.01; p<0.01) and similar intercept (a=0.08/0.05; p<0.01).

Hydrology and
Earth System
Sciences
Discussions
Open Access
EGU
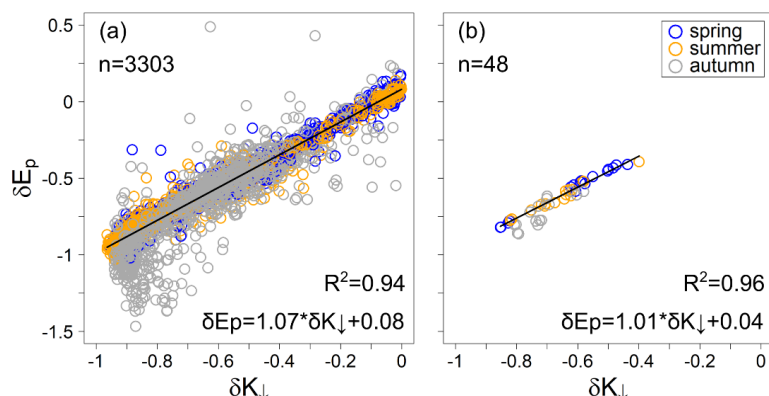
Figure 14: δE_p in dependence of $\delta K_\downarrow$ in both streets at all measurement locations in all three seasons. (a) Non-aggregated hourly data, (b) daily average values. Ten data points from ES in winter with $\delta E_p < -1.5$ are not displayed in (a) for better visualization.

370   By equalizing Eq. (8) with the regression equation and resolving for $E_{p,s}$, we can simulate $E_{p,s}$ with $\delta K_\downarrow$ and $E_{p,r}$ as the only

input variables for hourly and daily rates (Eq. 10).

$$\frac{E_{p,s} - E_{p,r}}{|E_{p,r}|} = a + b * \delta K_\downarrow \ [-] \tag{10}$$

This procedure allows to calculate $E_{p,s}$ at any location in a city based on simulated (derived from the simulated sky view factor

(e.g. Middle et al., 2018) or observed short wave time series and observations at a reference climate station to derive $E_{p,r}$.

375   **4 Discussion**

4.1 Short wave radiation

The observed shading ($\delta K_\downarrow$) at each measurement location represents the sun path plotted in the binary fish eye images very

well (Fig. 15). However, the mean diurnal variation of $\delta K_\downarrow$ at one measurement location may not represent the sun path exactly.

This might be due to the position adjustments of the trailer when parking cars were blocking the target location. In special

380   cases, when the sky was partly clouded, we observed cloudy conditions in the street but clear sky conditions at the roof top

station during the 4-minute-measurment interval. In such a case we got a low $\delta K_\downarrow$ even if there was no shade created by trees

or a wall. Vice versa, we got positive $\delta K_\downarrow$ when we had cloudy conditions at the roof top station, but sunny conditions in the

streets.
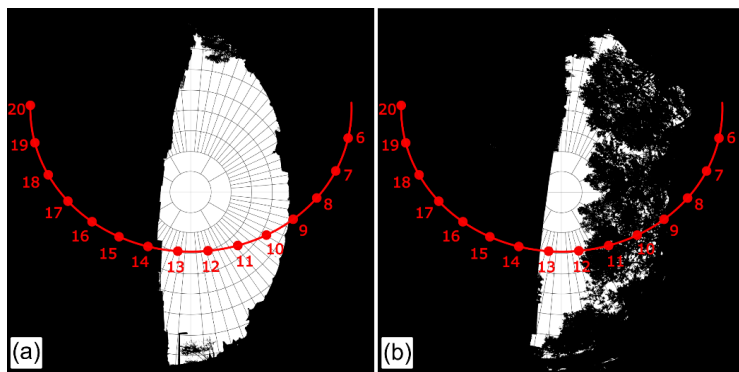
385   **Figure 15: Sun path at (a) n_W2 and (b) v_W1 in HS at 2016/07/20 which is the middle day of the summer observation period in HS.**

4.2 Long wave radiation/ infrared surface temperatures

The longwave radiation observations and evaluation method presented in this study is a rough approximation to direct longwave radiation measurements and inhibits several uncertainties. Errors in estimating incoming longwave radiation as

390 described in Eq. (3)–(6) might be induced by taking ground surface infrared radiation temperature observed at one small spot at one measurement location as representative for the entire ground seen by all four lateral sensors: In Eq. (4) and (5), we used $T_{s,ground}$ to correct the bulk surface temperature observed by the lateral pointing sensors for the fraction contributed by the ground appearing in their FOVs. But the fractions of ground seen by the lateral sensors might have completely different infrared radiation surface temperatures due to vegetation or deviating antecedent expositions to shortwave radiation. When the ground

395 screened by the lateral sensors is overall warmer than the observed $T_{s,ground}$, $L_{\downarrow s}$ is overestimated and vice versa.

When calculating the mean incoming infrared radiation surface temperature $\overline{T_{s\downarrow}}$ (Eq. 6), the upper parts of walls and trees and the lower parts of the sky are overrepresented since they appear in one or multiple lateral sensors and in addition in the upward pointing sensor. This overlapping of surfaces is caused by the technical issue of the upward pointing sensor being fixed lower on the trailer than the lateral pointing sensors. We expect this error to be small compared to the error induced by the ground

400 infrared radiation temperature correction.

We derived $\overline{T_{s\downarrow}}$ from the four lateral and the upward pointing sensor because we wanted to represent the hemisphere and the sky view factor at the measurement locations. But the so derived $\overline{T_{s\downarrow}}$ leads to an underestimation of $L_{\downarrow s}$ in Eq. (7) because the sky "seen" by the upward pointing sensor overall decreases $\overline{T_{s\downarrow}}$ compared to $T_{s\downarrow}$ from the lateral sensors, where the proportion of walls is higher. Underestimation of $L_{\downarrow s}$ is larger for measurement locations with higher SVFs. However, despite these

405 uncertainties in our observation and evaluation method, the $L_{\downarrow s}$ estimates seem to be plausible. Comparing $L_{\downarrow s}$ with $L_{\downarrow r}$, a clear influence of the urban surroundings on incoming longwave radiation with $L_{\downarrow s}$ being nearly always above $L_{\downarrow r}$ becomes visible (Fig. 9). This positive contribution of horizon obstructions to incoming longwave radiation in general is also described in other studies (Blankenstein & Kuttler, 2004; Nunez et al., 2000; and Verseghy & Munro,1989). Therefore, the scatter in the $L_{\downarrow s}$ observations for each season (in addition to changes in atmospheric counter radiation) is mainly related with the different sky

410 view factors at the measurement locations. We found overall negative correlations between Ψ_{sky} and $\Delta L_{\downarrow}$ within each street in each season, comparable to those described by Blankenstein & Kuttler (2004), Nunez et al. (2000) and Verseghy and Munro (1989). Since we observed only daytime incoming longwave radiation, we identified an influence of the exposition of the measurement locations and their adjacent walls to $K_{\downarrow}$. Such an influence was also mentioned by Verseghy and Munro (1989). For example, for sunny conditions in summer in ES, the direct solar radiation to the northern wall in the non-vegetated section

415 caused higher $\Delta L_{\downarrow}$ at n_N1 and n_S1 compared to v_N3 and v_S2 which had very similar sky view factors but were shaded by the vegetation (results not shown). In contrast, when the sky is very cloudy, the atmosphere has a higher emissivity compared to clear sky conditions in the same season while the surface temperature of the walls stays relatively cool due to reduced short wave radiation input. Consequently, $\Delta L_{\downarrow}$ for cloudy conditions (cc < 0.5) was close to or little below zero at all measurement locations in all seasons and was hardly dependent on Ψ_{sky}.

420 Further validation and investigation of our longwave radiation observation and estimation method would be interesting but is beyond the scope of this study. Since E_p was second most sensitive to changes in $\delta L_{\downarrow}$, we recommend to further investigate the effect of longwave radiation emission from the surroundings when investigating E_p in an urban environment.

4.3 Wind

Wind speed in the streets was usually below roof top wind speed. This was expected considering the additional roughness in

425 the streets compared to the roughness at the roof top station (Nakamura & Oke, 1988). Sometimes, wind speed in the streets exceeded rooftop wind speed (Fig. 9). Due to the spatial distance between the rooftop station and the two streets and the short measurement intervals of four minutes, wind gusts may only have been observed in the streets but not at the roof top station (but also vice versa). Another reason for positive Δu might be traffic at calm days. It is also possible, that roof top station and

streets in Freiburg might be situated in two different mountain-plain wind systems leading to different wind dynamics,

430   especially in the morning and in the evening. Another reason could simply be an error in correction of observation height of reference wind speed observations. Nakamura and Oke (1988) observed wind speed in Kyoto, Japan, in August 1983 and August 1984 in an E-W oriented canyon and compared it to observations from a reference station on top of a building directly adjacent to the canyon. For their overall measurements they found $u_s = 2/3*u_r$. But they also observed positive Δu values especially for low velocities of $u_r < 1$ m^{-1} even though their reference data was taken right above the canyon, was not corrected

435   for measurement height and their data was analyzed as 10-minute means from 1-minute measurements or 10-second measurements.

4.4 Air temperature

The cooling effect caused by shading that we observed in HS in summer, is similar to that reported by Shashua-Bar & Hoffman (2000). They investigated the cooling effect of trees in Tel Aviv during a sunny and hot period. They compared air temperature

440   within several streets with trees against air temperature observations at relatively open spaces at the entrance of each street. For two N-S-oriented streets characterized as urban canyons with trees along the sidewalks, they observed the largest difference in air temperature for both streets at 15:00h (solar noon was at 14:20h) when ΔT_a was -1.3 K for one and -2.3 K for the other street. This is very similar to our findings. Shashua-Bar & Hoffman (2000) also found that the cooling effect of green spaces and vegetated streets is perceivable up to 100 m from the site boundary. They observed an exponential decay of the cooling

445   effect from the border of the green area into the surrounding area which for example was an intersecting road without trees. This means that air temperature in the non-vegetated section in HS might be affected by the cooler air in the vegetated section and that the cooling effect of the trees in HS might be more intense when compared to a non-vegetated section further away from the vegetated section.

4.5 Potential evapotranspiration

450   Sensitivity analyses have already been applied to Eq. (1) in several other studies. In most of these studies, the focus is on long term changes in E_p as a reaction to climate change (Ambas & Baltas, 2012; Bormann, 2012; Gong et al., 2006; Sharifi & Dinpashoh, 2014; Tabari & Talaee, 2014) or on potential errors of E_p estimations due to inaccurate observations of input variables (Beven, 1979; Bois & Pieri, 2005; Debnath et al., 2015). The OAAT approach is a common method to perform a sensitivity analysis. One input variable may be changed within a range of ± 20 % with an interval of ±5 % while the other

455   variables are kept constant (Gong et al., 2006; Sharifi & Dinpashoh, 2014; Tabari & Talaee, 2014). In contrast, after exchanging reference against street observations during our OAAT approach, we observed changes in wind speed and incoming shortwave radiation that were mostly below -20% and rarely positive. Changes in incoming longwave radiation were mostly positive with a maximum change of + 23 % (Fig. 9). This shows, that the assumed changes of the input variables with a range of ± 20 % are not suitable for a sensitivity analyses of E_p in an urban context. To our knowledge, the sensitivity to $L_\downarrow$ has not yet been

460   investigated directly in other studies.

Beven (1979) studied the sensitivity of Penman-Monteith actual evapotranspiration (E_a) estimates of a grass surface on changes in the input variables on a sub daily time scale. For his analysis, Beven (1979) took the changes in input variables and in E_a that appeared from time step to time step with an hourly time interval. For daytime data, Beven (1979) found that E_a was most sensitive to changes in net radiation and that the seasonal variation in the sensitivity coefficients was small relative to changes

465   in predicted E_a. The mean monthly mid-day sensitivity coefficient for hourly net radiation found by Beven was around 0.7 for the whole observation period from May to November 1976. Since the observations took place at an unobstructed site, net radiation may have been mainly influenced by changes in the incoming shortwave radiation flux due to changes in cloud cover. We did not analyze the sensitivity of $E_{p,r}$ to the reference input variables or to net radiation comparable to Beven's (1979) approach but the very high correlation coefficient between $E_{p,r}$ and $K_{\downarrow,r}$ ($r_{K\downarrow,r} = 0.96$) provides an indication to the sensitivity

Hydrology and
Earth System
Sciences
Discussions
EGU
Open Access

470   of E_p to variations in $K_\downarrow$. When considering the street observations, short wave radiation becomes even more important since the correlation coefficients for all other variables except incoming longwave radiation are lower compared to correlation coefficients between $E_{p,r}$ and its input variables.

   Our findings reflect the results of the study conducted by Litvak & Pataki (2016) who found high sensitivity of ET_0 to shade provided by trees. They calculated daily k_{mc} values from $ET_{0(in\ situ)} = k_{mc}ET_0$ based on the LCM method (Costello et al., 2000),

475   where daily $ET_{0(in\ situ)}$ was derived from in situ meteorological measurements on eight urban lawns and daily ET_0 was derived from a reference weather station. According to the regression approach by Litvak & Pataki (2016), they derived a $\delta K_\downarrow = -0.44$ for 83.7 % tree cover. This lies at the upper end of the range of our observed daily $\delta K_\downarrow$ values and means that daily $K_\downarrow$ on a greenspace 83.7 % tree cover would be expected to be 56 % of $K_{\downarrow r}$. This seems quite plausible since shade by trees is less "intense" than shade by building walls and in addition, when the sun is low, short wave radiation may pass below the treetop.

480   For unshaded lawns, Litvak & Pataki (2016) did not find a significant difference between $ET_{0(in\ situ)}$ and ET_0. We did not have measurement locations that were unshaded during the whole day but for hours in spring and summer with $\delta K_\downarrow > -0.05$, δE_p ranged between -0.16 and 0.17 and the difference between $E_{p,s}$ and $E_{p,r}$ was not significant as well (results not shown).

   We did not investigate the sensitivity of δE_p during nighttime hours, when shortwave radiation cannot play a role in governing E_p rates. But the contribution of nighttime E_p to total daily (24h) E_p is very low (Fig. 8 and Table 3) and the error when using

485   Eq. (10) to simulate daily (24h) $E_{p,s}$ rates is expected to be very small. When estimating $E_{p,s}$ with an hourly time step, we suggest to use reference E_p for nighttime hours.

   The influence of changes in the other variables on E_p was only small. Their mixed effect on δE_p is represented by the intercept of our hourly and daily regression curve, respectively. This mixed effect might be changed for areas with a different street design (wider streets, more/less vegetation, heterogenic arrangement of buildings) or in a different climate zone. Especially in

490   cities that are very densely built and where streets are shaded most of the day, E_p might become more sensitive to changes in other variables than $K_\downarrow$. On the other hand, we can assume that areas between buildings in those cities do not contribute very much to evapotranspiration. The sensitivity of E_p to changes in the input variables also changes with different climate. Since changes in $K_\downarrow$ will be the most intense within an urban area compared to changes in the other variables, we assume that the overall relationship between $K_\downarrow$ and E_p will not be changed, but that the mixed effect of the other variables may be altered.

495   More observations are needed to investigate a wider range of urban conditions. Especially sites that are shaded/never shaded for the whole day should be included in future studies to complete the range of daily $\delta K_\downarrow$.

5 Conclusion

   We collected a unique and comprehensive data set of urban micro-meteorological variables that are needed to calculate FAO-56 Penman-Monteith reference evapotranspiration at a high spatio-temporal resolution in an urban environment. This data set

500   allowed for analyzing the influence of urban microclimatic conditions in an urban canyon on potential evapotranspiration. According to our results, potential evapotranspiration is most sensitive to changes in incoming shortwave radiation. Changes in incoming shortwave radiation on street level are induced by shading of trees and buildings which lead to an overall decrease in potential evapotranspiration in the streets compared to potential evapotranspiration at a reference station on a rooftop. The strong sensitivity to changes in incoming shortwave radiation enabled to estimate the change in potential evapotranspiration

505   in dependence of the change in incoming shortwave radiation as the only input variable. Incoming shortwave radiation on street level can easily be simulated with a digital elevation model of the city of interest and a common GIS software (e.g. with the solar radiation tool by ArcGIS). The dependence of potential evapotranspiration on street level on changes in incoming shortwave radiation causes a strong variability in the diurnal variation of potential evapotranspiration at the different measurement locations in the street which is consequently affected by their exposition to incoming shortwave radiation. This

510   should be taken into account when considering green or blue infrastructure as tools for heat mitigation in cities. In summary,

the presented procedure for the downscaling of reference E_p to the urban canyon enables the improvement of urban hydrologic modelling with regard to more precise estimates of potential evapotranspiration which will be an important tool for the simulation and prediction of urban heat mitigation measures.

Author contribution

515   MK, TS and MW conceptualized the study and MK developed the measurement design. MK collected, analysed and visualised the data. MK prepared and wrote the manuscript. MW and TS revised the manuscript.

Competing interests

The authors declare that they have no conflict of interest; however, the author Markus Weiler is a member of the editorial board of the journal.

References

Allen, R. G., Pereira, L. S., Raes, D. and Smith, M.: Crop Evapotranspiration - Guidelines for Computing Crop Water
530   Requirements - FAO Irrigation and Drainage Paper 56., FAO - Food and Agriculture Organization of the United Nations, Rome, Italy., 1998.

Ambas, V. T. and Baltas, E.: Sensitivity analysis of different evapotranspiration methods using a new sensitivity coefficient, Glob. Nest J., 14(3), 335–343, doi:10.30955/gnj.000882, 2012.

Bach, P. M., Rauch, W., Mikkelsen, P. S., McCarthy, D. T. and Deletic, A.: A critical review of integrated urban water
535   modelling - Urban drainage and beyond, Environ. Model. Softw., 54, 88–107, doi:10.1016/j.envsoft.2013.12.018, 2014.

Bärring, L., Mattsson, J. O. and Lindqvist, S.: Canyon geometry, street temperatures and urban heat island in malmö, sweden, J. Climatol., 5(4), 433–444, doi:10.1002/joc.3370050410, 1985.

Berthier, E., Dupont, S., Mestayer, P. G. and Andrieu, H.: Comparison of two evapotranspiration schemes on a sub-urban site, J. Hydrol., 328(3–4), 635–646, doi:10.1016/j.jhydrol.2006.01.007, 2006.

540   Beven, K.: A sensitivity analysis of the Penman-Monteith actual evapotranspiration estimates, J. Hydrol., 44(3–4), 169–190, doi:10.1016/0022-1694(79)90130-6, 1979.

Blankenstein, S. and Kuttler, W.: Impact of street geometry on downward longwave radiation and air temperature in an urban environment, Meteorol. Zeitschrift, 13(5), 373–379, doi:10.1127/0941-2948/2004/0013-0373, 2004.

Bois, B. and Pieri, P.: Sensitivity analysis of the Penman-Monteith evapotranspiration formula and comparison of empirical
545   methods used in viticulture soil water balance., in XIV International GESCO Viticulture Congress, 23-17 August 2005, pp. 1–

6, Groupe d'Etude des Systemes de COnduite de la vigne (GESCO), Geisenheim, Germany. [online] Available from: https://www.cabdirect.org/cabdirect/abstract/20053213723 (Accessed 3 January 2020), 2005.

Bonneau, J., Fletcher, T. D., Costelloe, J. F. and Burns, M. J.: Stormwater infiltration and the 'urban karst' – A review, J. Hydrol., 552, 141–150, doi:10.1016/j.jhydrol.2017.06.043, 2017.

550   Bormann, H.: Sensitivity analysis of 18 different potential evapotranspiration models to observed climatic change at German climate stations, Clim. Change, 104(3–4), 729–753, doi:10.1007/s10584-010-9869-7, 2011.

Bourbia, F. and Awbi, H. B.: Building cluster and shading in urban canyon for hot dry climate Part 2: Shading simulations, Renew. Energy, 29(2), 291–301, doi:10.1016/S0960-1481(03)00171-X, 2004.

Brandsma, T. and Wolters, D.: Measurement and statistical modeling of the urban heat island of the city of Utrecht
555   (Netherlands), J. Appl. Meteorol. Climatol., 51(6), 1046–1060, doi:10.1175/JAMC-D-11-0206.1, 2012.

Chen, L., Ng, E., An, X., Ren, C., Lee, M., Wang, U. and He, Z.: Sky view factor analysis of street canyons and its implications for daytime intra-urban air temperature differentials in high-rise, high-density urban areas of Hong Kong: a GIS-based simulation approach, Int. J. Climatol., 32(1), 121–136, doi:10.1002/joc.2243, 2012.

Conrads, L. A. and Van Der Hage, J. C. H.: A new method of air-temperature measurement in urban climatological studies,
560   Atmos. Environ., 5(8), 629–635, doi:10.1016/0004-6981(71)90119-3, 1971.

Costello, L., Matheny, N., Clark, J. and Jones, K.: A Guide to Estimating Irrigation Water Needs of Landscape Plantings in California, the Landscape Coefficient Method and Wucols III, University of California Cooperative Extension; California Department of Water Resources, Sacramento, CA. [online] Available from: http://www.water.ca.gov/wateruseefficiency/docs/wucols00.pdf, 2000.

565   Debnath, S., Adamala, S. and Raghuwanshi, N. S.: Sensitivity Analysis of FAO-56 Penman-Monteith Method for Different Agro-ecological Regions of India, Environ. Process., 2(4), 689–704, doi:10.1007/s40710-015-0107-1, 2015.

Dimoudi, A., Kantzioura, A., Zoras, S., Pallas, C. and Kosmopoulos, P.: Investigation of urban microclimate parameters in an urban center, Energy Build., 64, 1–9, doi:10.1016/j.enbuild.2013.04.014, 2013.

Elliott, A. H. and Trowsdale, S. A.: A review of models for low impact urban stormwater drainage, Environ. Model. Softw.,
570   22(3), 394–405, doi:10.1016/j.envsoft.2005.12.005, 2007.

Erell, E. and Williamson, T.: Intra-urban differences in canopy layer air temperature at a mid-latitude city, Int. J. Climatol., 27(9), 1243–1255, doi:10.1002/joc.1469, 2007.

Fletcher, T. D., Andrieu, H. and Hamel, P.: Understanding, management and modelling of urban hydrology and its consequences for receiving waters: A state of the art, Adv. Water Resour., 51, 261–279, doi:10.1016/j.advwatres.2012.09.001,
575   2013.

Gong, L., Xu, C. yu, Chen, D., Halldin, S. and Chen, Y. D.: Sensitivity of the Penman-Monteith reference evapotranspiration to key climatic variables in the Changjiang (Yangtze River) basin, J. Hydrol., 329(3–4), 620–629, doi:10.1016/j.jhydrol.2006.03.027, 2006.

Grimmond, C. S. B. and 0ke, T. R.: An Evapotranspiration-Interception Model for Urban Areas, WATER Resour. Res., 27(7),
580   1739–1755, 1991.

Grimmond, C. S. B. and Oke, T. R.: Evapotranspiration rates in urban areas, IAHS-AISH Publ., 235–243 [online] Available from: http://www.met.reading.ac.uk/micromet/publications/GrimmondOkeIAHS1999.pdf, 1999.

Heusinkveld, B. G., Steeneveld, G. J., Van Hove, L. W. A., Jacobs, C. M. J. and Holtslag, A. A. M.: Spatial variability of the Rotterdam urban heat island as influenced by urban land use, J. Geophys. Res., 119(2), 677–692, doi:10.1002/2012JD019399,
585   2014.

Holst, J. and Mayer, H.: Impacts of street design parameters on human-biometeorological variables, Meteorol. Zeitschrift, 20(5), 541–552, doi:10.1127/0941-2948/2011/0254, 2011.

Lee, H., Holst, J. and Mayer, H.: Modification of human-biometeorologically significant radiant flux densities by shading as local method to mitigate heat stress in summer within urban street canyons, Adv. Meteorol., 13, doi:10.1155/2013/312572,
590   2013.

Lerner, D. N.: Identifying and quantifying urban recharge: A review, Hydrogeol. J., 10(1), 143–152, doi:10.1007/s10040-001-0177-1, 2002.

Litvak, E. and Pataki, D. E.: Evapotranspiration of urban lawns in a semi-arid environment: An in situ evaluation of microclimatic conditions and watering recommendations, J. Arid Environ., 134, 87–96, doi:10.1016/j.jaridenv.2016.06.016, 2016.

595

Matsui, H. and Osawa, K.: Calibration effects of the net longwave radiation equation in Penman-type methods at Tateno, Japan, Hydrol. Res. Lett., 9(4), 113–117, doi:10.3178/hrl.9.113, 2015.

Matzarakis, A., Rutz, F. and Mayer, H.: Modelling Radiation fluxes in simple and complex environments – Application of the RayMan model, Int. J. Biometeorol., 51, 323–334, doi:10.1007/s00484-006-0061-8, 2007.

600 Matzarakis, A., Rutz, F. and Mayer, H.: Modelling radiation fluxes in simple and complex environments: Basics of the RayMan model, Int. J. Biometeorol., 54(2), 131–139, doi:10.1007/s00484-009-0261-0, 2010.

Middel, A., Lukasczyk, J., Maciejewski, R., Demuzere, M. and Roth, M.: Sky View Factor footprints for urban climate modeling, Urban Clim., 25(May), 120–134, doi:10.1016/j.uclim.2018.05.004, 2018.

Mitchell, V. G., Mein, R. G. and McMahon, T. A.: Modelling the urban water cycle, Environ. Model. Softw., 16(7), 615–629, 605 doi:10.1016/S1364-8152(01)00029-9, 2001.

Nakamura, Y. and Oke, T. R.: Wind, temperature and stability conditions in an east-west oriented urban canyon, Atmos. Environ., 22(12), 2691–2700, doi:10.1016/0004-6981(88)90437-4, 1988.

Norton, B. A., Coutts, A. M., Livesley, S. J., Harris, R. J., Hunter, A. M. and Williams, N. S. G.: Planning for cooler cities: A framework to prioritise green infrastructure to mitigate high temperatures in urban landscapes, Landsc. Urban Plan., 134, 127–610 138, doi:10.1016/j.landurbplan.2014.10.018, 2015.

Nouri, H., Beecham, S., Kazemi, F. and Hassanli, A. M.: A review of ET measurement techniques for estimating the water requirements of urban landscape vegetation, Urban Water J., 10(4), 247–259, doi:10.1080/1573062X.2012.726360, 2013.

Nunez, M., Eliasson, I. and Lindgren, J.: Spatial variation of incoming longwave radiation in Göteborg, Sweden, Theor. Appl. Climatol., 67(3–4), 181–192, doi:10.1007/s007040070007, 2000.

615 Offerle, B., Eliasson, I., Grimmond, C. S. B. and Holmer, B.: Surface heating in relation to air temperature, wind and turbulence in an urban street canyon, Boundary-Layer Meteorol., 122(2), 273–292, doi:10.1007/s10546-006-9099-8, 2007.

Oke, T. R.: Street Design and Urban Canopy Layer Climate, Energy Build., 11, 103–113, 1988.

Oke, T. R.: Towards better scientific communication in urban climate, Theor. Appl. Climatol., 84(1–3), 179–190, doi:10.1007/s00704-005-0153-0, 2006.

620 Rajkovich, N. B. and Larsen, L.: A bicycle-based field measurement system for the study of thermal exposure in Cuyahoga county, Ohio, USA, Int. J. Environ. Res. Public Health, 13(2), doi:10.3390/ijerph13020159, 2016.

Rodriguez, F., Andrieu, H. and Zech, Y.: Evaluation of a distributed model for urban catchments using a 7-year continuous data series, Hydrol. Process., 14(5), 899–914, doi:10.1002/(SICI)1099-1085(20000415)14:5<899::AID-HYP977>3.0.CO;2-R, 2000.

625 Rodriguez, F., Andrieu, H. and Morena, F.: A distributed hydrological model for urbanized areas – Model development and application to case studies, J. Hydrol., 351(3–4), 268–287, doi:10.1016/j.jhydrol.2007.12.007, 2008.

Salata, F., Golasi, I., de Lieto Vollaro, R. and de Lieto Vollaro, A.: Urban microclimate and outdoor thermal comfort. A proper procedure to fit ENVI-met simulation outputs to experimental data, Sustain. Cities Soc., 26, 318–343, doi:10.1016/j.scs.2016.07.005, 2016.

630 Salvadore, E., Bronders, J. and Batelaan, O.: Hydrological modelling of urbanized catchments: A review and future directions, J. Hydrol., 529(P1), 62–81, doi:10.1016/j.jhydrol.2015.06.028, 2015.

Schirmer, M., Leschik, S. and Musolff, A.: Current research in urban hydrogeology - A review, Adv. Water Resour., 51, 280–291, doi:10.1016/j.advwatres.2012.06.015, 2013.

Sharifi, A. and Dinpashoh, Y.: Sensitivity Analysis of the Penman-Monteith reference Crop Evapotranspiration to Climatic 635 Variables in Iran, Water Resour. Manag., 28(15), 5465–5476, doi:10.1007/s11269-014-0813-x, 2014.

Shashua-Bar, L. and Hoffman, M. E.: Vegetation as a climatic component in the design of an urban street. An empirical model for predicting the cooling effect of urban green areas with trees, Energy Build., 31(3), 221–235, doi:10.1016/S0378-7788(99)00018-3, 2000.

640 Tabari, H. and Talaee, P. H.: Sensitivity of evapotranspiration to climatic change in different climates, Glob. Planet. Change, 115, 16–23, doi:10.1016/j.gloplacha.2014.01.006, 2014.

Tsin, P. K., Knudby, A., Krayenhoff, E. S., Ho, H. C., Brauer, M. and Henderson, S. B.: Microscale mobile monitoring of urban air temperature, Urban Clim., 18, 58–72, doi:10.1016/j.uclim.2016.10.001, 2016.

Unger, J., Sümeghy, Z. and Zoboki, J.: Temperature cross-section features in an urban area, Atmos. Res., 58(2), 117–127, doi:10.1016/S0169-8095(01)00087-4, 2001.

645 United Nations: World Urbanization Prospects : The 2018 Revision (ST/ESA/SER.A/420), United Nations, Now York. [online] Available from: https://population.un.org/wup/Publications/Files/WUP2018-Report.pdf, 2018.

Verseghy, D. L. and Munro, D. S.: Sensitivity studies on the calculation of the radiation balance of urban surfaces: II. Longwave radiation, Boundary-Layer Meteorol., 48, 1–18, doi:10.1007/BF00121780, 1989.

Voogt, J. A. and Oke, T. R.: Radiometric temperatures of urban canyon walls obtained from vehicle traverses, Theor. Appl.
650 Climatol., 60(1–4), 199–217, doi:10.1007/s007040050044, 1998.

Zoppou, C.: Review of urban storm water models, Environ. Model. Softw., 16(3), 195–231, doi:10.1016/S1364-8152(00)00084-0, 2001.